

Performance Characterization of an Indoor Localization System with LTE Code and Carrier Phase Measurements and an IMU

Ali A. Abdallah¹, Kimia Shamaei¹, and Zaher M. Kassas^{1,2}

¹ Department of Electrical Engineering and Computer Science, University of California, Irvine, CA, USA

Email: {abdalla2, kshamaei}@uci.edu

² Department of Mechanical and Aerospace Engineering, University of California, Irvine, CA, USA

Email: zkassas@ieee.org

Abstract—The Performance of cellular long-term evolution (LTE) signals for indoor localization is evaluated. Two different designs of LTE software-defined receivers (SDRs), namely a code phase-based receiver and a carrier phase-based receiver, are presented and assessed experimentally indoors with LTE signals. A base/navigator framework is presented to deal with the unknown clock biases of the LTE eNodeBs. In this framework, the base receiver is placed outdoors, has knowledge of its own position, and makes pseudorange measurements to eNodeBs in the environment whose positions are known. The base transmits these pseudoranges to the indoor navigating receiver, which is also making pseudorange measurements to the same eNodeBs. The navigating receiver differences the base's and navigator's pseudoranges; hence, the unknown eNodeBs' biases are eliminated. The navigator receiver is equipped with an inertial measurement unit (IMU), and the LTE pseudoranges and IMU measurements are tightly coupled using an extended Kalman filter (EKF). Two sets of experimental results are presented. First, it is demonstrated that the standalone carrier phase-based receiver yielded a more precise navigation solution than the code phase-based receiver, specifically a two-dimensional (2-D) position root mean-squared error (RMSE) of 5.09 m versus 11.76 m for an indoor trajectory of 109 m traversed in 50 seconds. Second, it is demonstrated that coupling the IMU with the carrier phase-based LTE receiver reduced the 2-D position RMSE to 2.92 m. Moreover, it is demonstrated that the proposed LTE-IMU system yielded a maximum error of 5.60 compared to 22.53 m for the IMU-only.

Index Terms—LTE, IMU, opportunistic navigation, indoor localization.

I. INTRODUCTION

According to the U.S. environmental protection agency, the average American spend 93% of their time indoors. This has dramatically increased the number of emergency calls originating indoors [1]. This makes accurate indoor localization more important than ever to: (1) localize the emergency caller and (2) localize the emergency responder in their mission indoors.

Over the past decades, global navigation satellite systems (GNSS) have provided sufficiently accurate outdoor localization for many applications, e.g., surveying, transportation, aviation, etc. However, the received GNSS signals are highly attenuated indoors, which makes them practically

This work was performed under the financial assistance award 70NANB17H192 from U.S. Department of Commerce, National Institute of Standards and Technology (NIST).

unusable for indoor applications. Besides, GNSS signals' low bandwidth makes them susceptible to multipath, which severely affects the signals indoors.

Several approaches have been proposed to address the challenge of indoor localization, e.g., visible light communication [2], [3], active radio frequency identifications (RFIDs) [4], [5], ultra wideband (UWB) signals [6], and using different sensors such as inertial measurements units (IMUs) [7], lidar [8], and cameras [9]. These approaches; however, can be impractical or of limited accuracy in emergency situations, since: (1) they require pre-deployed infrastructure (e.g., UWB), (2) they may not work properly in some emergency conditions (e.g., cameras in smoke), or (3) they require aiding sources, otherwise their solution will diverge over time (e.g., IMU).

Recent research has focused on exploiting signals of opportunity (SOPs) for navigation. SOPs are ambient radio frequency (RF) signals, which are not designed for navigation; but, they are freely available in GNSS-challenged environments and can be exploited for navigation purposes. AM/FM [10], [11], digital television [12], Wi-Fi [13], [14], cellular [15], [16], and low Earth orbit satellites [17]–[19] are examples of SOPs.

Among different SOPs, cellular long-term evolution (LTE) signals are very promising for indoor localization, particularly in case of emergency, due to their desirable characteristics: ubiquity, geometric diversity, large transmission bandwidth (i.e., up to 20 MHz), and high received power.

The achievable ranging and localization accuracy of different LTE reference signals have been analyzed in the literature [20], [21] and several software-defined receivers (SDRs) have been proposed to exploit LTE signals for navigation [22]–[24]. The navigation observables of these LTE SDRs have been used in different navigation frameworks, both indoors and outdoors, where experimental results demonstrated meter-level localization accuracy on ground-based receivers with real and laboratory emulated LTE signals [25]–[29] and sub-meter-level accuracy on aerial vehicle-based receivers with real LTE signals [30]. This paper presents two different LTE receivers for indoor navigation: (1) a code phase-based receiver and (2) a carrier phase-based receiver. Experimental results are provided to compare these receivers using real LTE signals. The paper

TABLE I
LIST OF POSSIBLE LTE DOWNLINK BANDWIDTH CONFIGURATIONS

Bandwidth (MHz)	Total number of subcarriers	Number of subcarriers used
1.4	128	72
3	256	180
5	512	300
10	1024	600
15	1536	900
20	2048	1200

presents a base/navigator framework to eliminate the unknown LTE eNodeBs' biases. In this framework, the base receiver is placed outdoors, has knowledge of its own position, and makes pseudorange measurements to eNodeBs in the environment whose positions are known. The base transmits these pseudoranges to the indoor navigating receiver, which is also making pseudorange measurements to the same eNodeBs. The navigating receiver differences the base's and navigator's pseudoranges; hence, the unknown eNodeBs' biases are eliminated. Moreover, a tightly-coupled extended Kalman filter (EKF)-based LTE-IMU system is presented, where the LTE pseudoranges aid the IMU. The proposed navigation framework is evaluated experimentally in an indoor trajectory of 109 m with a tactical-grade IMU and using 5 LTE base stations (also known as evolved Node Bs or eNodeBs). The results demonstrated a two-dimensional (2-D) position root mean squared-error (RMSE) of 2.92 m and a maximum error of 5.6 m.

The remainder of the paper is organized as follows. Section II characterizes the received signal model. Section III discusses both receivers' structures. Section IV describes the proposed base/navigator framework. Section V presents the experimental results, where the performance of both receivers are first compared, and the differences in performance are discussed. Then, the experimental results for the proposed framework in an indoor environment using real LTE signals are presented. Section VI concludes the paper.

II. SIGNAL MODEL

LTE uses orthogonal frequency division multiplexing (OFDM) modulation. The transmitted data symbols are mapped onto multiple carrier frequencies called subcarriers, with a subcarrier spacing of $\Delta f = 15$ kHz. The LTE downlink bandwidth can have different configurations as shown in Table I [31].

Several reference signals can be exploited from LTE signals and used for navigation purposes: (1) primary synchronization signal (PSS), (2) secondary synchronization signal (SSS), (3) positioning reference signal (PRS), and (4) cell-specific reference signals (CRS) [32]. The PSS and SSS, which are transmitted to provide the frame start time and the eNodeB's cell ID to the user equipment (UE), have a fixed bandwidth of 0.93 MHz. The PRS was introduced in LTE release-9 to allow proper ranging measurements of the UE from LTE eNodeBs. The CRS is mainly used for: (1) cell search and initial acquisition, (2) downlink channel quality measurements, and (3) downlink channel estimation for coherent demodulation/detection at the UE. The CRS bandwidth is the same as the transmission bandwidth of the

respective cell, which can be up to 20 MHz. This makes the CRS attractive for range measurements, especially in multipath environments. The CRS subcarrier allocation depends on the cell ID and the transmission antenna port. The transmitted OFDM signal from the u -th eNodeB at the k -th subcarrier and on the i -th symbol can be expressed as

$$Y_i^{(u)}(k) = \begin{cases} S_i^{(u)}(k), & \text{if } k = m\Delta_{CRS} + \nu_{i,N_{FD}^{Cell}}, \\ D_i^{(u)}(k), & \text{otherwise,} \end{cases} \quad (1)$$

where $S_i^{(u)}(k)$ represents the CRS sequence; $m = 0, \dots, M-1$; $M = \lfloor N_r/\Delta_{CRS} \rfloor$; N_r is the number of subcarriers carrying the data; $\Delta_{CRS} = 6$; $\nu_{i,N_{FD}^{Cell}}$ is a constant shift that depends on the cell ID and i ; and $D_i^{(u)}(k)$ represents some other data signals.

Due to wireless channel effect and receiver imperfections, i.e., synchronization, clock drift, Doppler frequency, and/or carrier frequency offset, the estimated received signal deviates from the transmitted signals. In the presence of this mismatch, the received signal at the i -th symbol can be written as [33]

$$R_i(k) = \sqrt{C} e^{j\pi e_f} e^{j2\pi(iN_t + L_{CP})e_f/N_c} e^{j2\pi e_\theta k/N_c} Y_i(k) H_i(k) + W_i(k), \quad k = 0, \dots, N_c - 1,$$

where C is the received signal power; $N_t = N_c + L_{CP}$; L_{CP} is the length of cyclic prefix (CP); $e_f = \frac{f_D}{\Delta f}$; f_D is the total carrier frequency offset due to clock drift, Doppler frequency, and oscillators' mismatch; $e_\theta = \hat{\theta} - \theta$ is the symbol timing error normalized by the sampling interval $T_s = T_{symbol}/N_c$; $T_{symbol} = \frac{1}{\Delta f}$; and $\hat{\theta}$ and θ are the normalized estimated and true symbol timings, respectively; $H_i(k)$ represents the channel frequency response; and $W_i(k) \sim \mathcal{CN}(0, \sigma^2)$, where $\mathcal{CN}(a, b)$ denotes the complex Gaussian distribution with mean a and variance b .

III. LTE RECEIVER STRUCTURES

In this section, the structures of two LTE receivers are presented: (1) a code phase-based receiver and (2) a carrier phase-based receiver. These receivers are an adaptation of the receiver originally introduced in [32].

A. LTE Code Phase-Based Receiver

The structure of the proposed LTE code phase-based receiver is shown in Fig. 1. In this receiver, an OFDM-based delay-locked loop (DLL) is used to track the code phase of the CRS. The proposed receiver has three main stages, where in each stage nodes A and B are connected to nodes 1, 2, or 3.

In the first stage, where nodes A and B are connected to node 1, a coarse estimate of the frame start time is obtained by acquiring the PSS and SSS. Then, the frame start time is used to control the fast Fourier transform (FFT) window timing. The CP elements are removed and an FFT is taken to convert the signal into the LTE frame structure.

In the second stage, the channel impulse response is estimated using the estimation of signal parameters by rotational invariance techniques (ESPRIT) algorithm [34]. The estimated TOA corresponding to the first path represents the line-of-sight (LOS) TOA and is used to refine

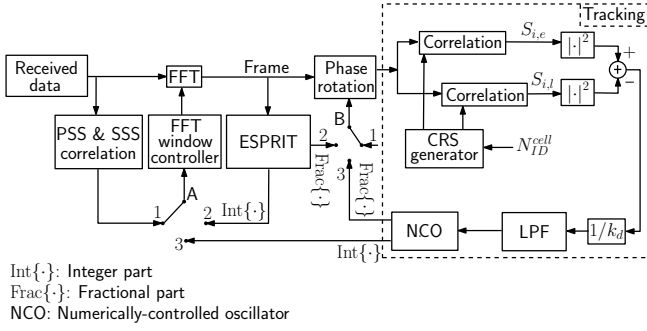


Fig. 1. Block diagram of the proposed LTE code phase-based receiver

the frame timing estimation. Then, the integer part of the estimated TOA is used to refine the FFT window timing and the fractional part is removed by a phase rotation in the frequency domain.

In the third stage (i.e., the tracking stage), a DLL is used to track the symbol timing. In a conventional DLL discriminator function (e.g., dot-product), correlation of the time-domain received signal with the locally generated early, late, and prompt replica of the signal is used to estimate the TOA error. However, the CRS is scattered in bandwidth, which makes it impractical to obtain its time-equivalent form. Hence, specialized DLL designed specifically for OFDM systems is used to track the CRS in LTE signals [24], [33]. In this DLL, the time-domain shift is represented as a phase rotation in the frequency-domain and the early and late correlations are obtained accordingly. Denoting the early and late correlations of the i -th received symbol with the locally generated CRS signal by $S_{i,e}$ and $S_{i,l}$, respectively, the DLL discriminator function can be defined as

$$D_i \triangleq |S_{i,e}|^2 - |S_{i,l}|^2 \triangleq M^2 C S_d(\tilde{e}_\theta, \xi) + N_{DLL},$$

where ξ is the correlator spacing, $S_d(\tilde{e}_\theta, \xi)$ is the normalized S-curve function, and N_{DLL} is the noise component of the discriminator function as defined in [32]. For small values of timing error, the discriminator function can be approximated by a linear function of the error with slope k_d . Therefore, normalizing the output of the discriminator function by k_d and passing it through a low-pass filter (LPF) provides an estimate of the timing error, which can be integrated to provide a refined estimate of the TOA.

B. LTE Carrier Phase-Based Receiver

The structure of the proposed LTE carrier phase-based receiver is shown in Fig. 2. In this receiver, a phase-locked loop (PLL) is implemented to track the phase of the CRS signal. Similar to the code phase-based receiver, the carrier-phase based receiver has 3 stages, where in each stage nodes A, B, and C are connected to nodes 1, 2, and 3, respectively. The first stage has common structure to the one discussed in Subsection III-A. In the second stage, along with the ESPRIT algorithm, an initial estimate of the Doppler frequency is obtained by defining $z(m)$ as

$$z(m) = R_{i+7}(k) R_{i+7}^*(k) S_{i+7}^*(k) S_i(k) \quad (2)$$

$$= C e^{j2\pi 7 N_t e_f / N_c} |H_i(k)|^2 + W'(k),$$

$$\text{for } k = m\Delta_{\text{CRS}} + \nu_{i, N_{ID}^{cell}}, \quad m = 0, \dots, M-1.$$

The above is obtained by assuming that the channel frequency response stays constant over one slot duration (i.e., 0.5 ms). Then, the initial Doppler frequency is estimated as

$$\hat{f}_D = \frac{1}{2\pi T_{\text{slot}}} \Delta\varphi, \quad (3)$$

$$\Delta\varphi \triangleq \arg \left[\sum_{m=0}^{M-1} z(m) \right]. \quad (4)$$

The initial Doppler estimate is removed from the received signal by a phase rotation on the time-domain received signal as

$$r(n) \leftarrow e^{-j2\pi \hat{f}_D n T_s} r(n),$$

where $r(n)$ is the received signal in the time-domain.

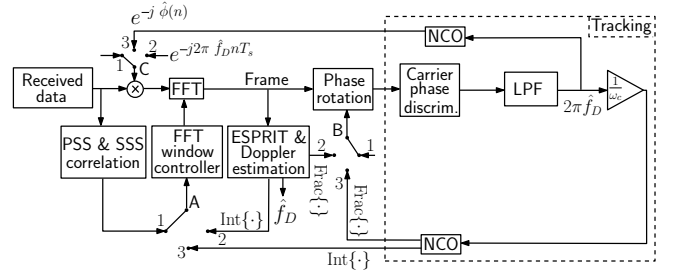


Fig. 2. Block diagram of the proposed LTE carrier phase-based receiver

In the third stage, where nodes A, B, and C are connected to 3, the receiver tracks the phase of the received signal and produces a fine estimate of the TOA using PLL. The carrier phase discriminator function of the PLL can be defined as

$$D_{\text{PLL}} = \arg \left[\sum_{m=0}^{M-1} R'(k) S^*(k) \right],$$

$$\text{for } k = m\Delta_{\text{CRS}} + \nu_{i, N_{ID}^{cell}}, \quad m = 0, \dots, M-1,$$

where $R'(k)$ is the frequency-domain received signal after removing the TOA and Doppler frequency estimate.

A second-order loop filter at the output of the discriminator function can be used [35], [36], which results in the rate of change of the carrier phase error $2\pi \hat{f}_D$ expressed in rad/s. By normalizing the results by angular carrier frequency ω_c , the rate of change of TOA can be obtained. Then, an integrator can be used to refine the estimate of TOA.

IV. INDOOR NAVIGATION FRAMEWORK

In this section, the proposed base/navigator navigation framework is presented. In this framework, LTE navigation observables are tightly coupled with IMU measurements using an EKF.

A. Base/Navigator Framework

One of the main challenges in navigation with LTE signals is the unknown clock biases of the LTE eNodeBs by the receiver. In this subsection, a base/navigator framework is proposed to address this challenge.

Fig. 3 describes the proposed framework, in which an LTE receiver, referred to as the base, is placed outdoors. The base receiver can be mounted on a fire truck or a police car, and can estimate its own position from GNSS. Note that the

base receiver installation is a one-time process that can be done prior to the emergency situation. The indoor navigator (e.g., emergency responder) is also equipped with an LTE receiver. The objective is to estimate the position of the navigator receiver \mathbf{r}_{nav} .

During the localization process, both the base and navigator receivers make pseudorange measurements to the same LTE eNodeBs located at $\{\mathbf{r}_{s_u}\}_{u=1}^U$, where U is the total number of eNodeBs in the environment. The base and navigator receivers' pseudorange measurements to the u -th eNodeB are denoted by $\rho_{\text{base}}^{(u)}$ and $\rho_{\text{nav}}^{(u)}$, respectively. The base receiver transmits its position and pseudorange measurements to the navigator receiver wirelessly. The navigator receiver differences its pseudorange estimates with the ones received from the base receiver to remove the unknown common term of eNodeBs' clock biases as shown in Fig. 3. The resulting measurements $\mathbf{z} \triangleq [z_1, \dots, z_U]^T$ are fed to the navigation filter to estimate the state vector.

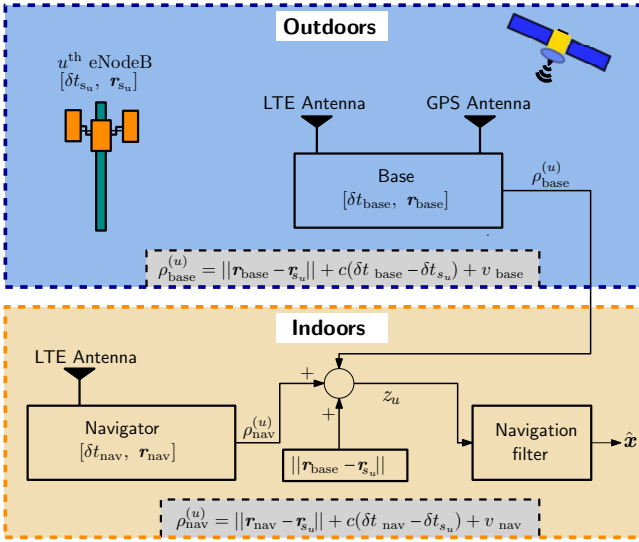


Fig. 3. The proposed base/Navigator Framework. The LTE base receiver, which is placed outdoors and transmits its location and pseudoranges to the indoor LTE navigator receiver. The navigator uses base's transmitted data to remove the unknown common term of eNodeB's clock bias.

B. LTE-IMU Tight Coupling Integration

The navigator receiver is assumed to be equipped with a barometer and an IMU. An EKF is used to fuse the IMU measurements with the base/navigator measurements \mathbf{z} in a tightly-coupled fashion as shown in Fig. 4. A barometer is used to estimate the navigator's altitude. Therefore, only 2-D position of the navigator is estimated in the EKF.

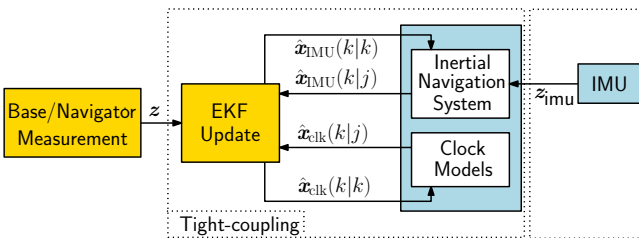


Fig. 4. Block diagram of the tightly-coupled LTE-IMU system.

1) *EKF State and Dynamic Model*: The navigator's state vector \mathbf{x} is defined as

$$\mathbf{x} = [\mathbf{x}_{\text{IMU}}^T, \mathbf{x}_{\text{clk}}^T]^T,$$

where \mathbf{x}_{IMU} and \mathbf{x}_{clk} are the IMU and clock state vectors, respectively.

The IMU state vector is defined as

$$\mathbf{x}_{\text{IMU}} \triangleq [\theta_z, \mathbf{r}^T, \dot{\mathbf{r}}^T, \mathbf{b}_a^T, b_{gz}]^T.$$

where θ_z is the orientation, $\dot{\mathbf{r}}$ is the 2-D velocity, and \mathbf{r} is the 2-D position of the IMU; \mathbf{b}_a represents the biases in the two accelerometers (x - and y -axes); and b_{gz} is the gyroscope's bias (around z -axis).

The clock state vector for the base/navigator framework is defined as

$$\mathbf{x}_{\text{clk}} \triangleq \mathbf{x}_{\text{clk}_{\text{nav}}} - \mathbf{x}_{\text{clk}_{\text{base}}} = [c\Delta\delta t, c\Delta\dot{\delta}t]^T,$$

where $\Delta\delta t \triangleq \delta t_{\text{nav}} - \delta t_{\text{base}}$; δt_{nav} and δt_{base} are the clock biases of the navigator and base receivers, respectively; $\Delta\dot{\delta}t \triangleq \dot{\delta}t_{\text{nav}} - \dot{\delta}t_{\text{base}}$; and $\dot{\delta}t_{\text{nav}}$ and $\dot{\delta}t_{\text{base}}$ are clock drifts of the navigator and base receivers, respectively.

The clock state vector \mathbf{x}_{clk} evolves according to

$$\mathbf{x}_{\text{clk}}(k+1) = \mathbf{F}_{\text{clk}} \mathbf{x}_{\text{clk}}(k) + \mathbf{w}_{\text{clk}}(k), \quad \mathbf{F}_{\text{clk}} \triangleq \begin{bmatrix} 1 & T \\ 0 & 1 \end{bmatrix},$$

where T is the sampling interval and \mathbf{w}_{clk} is the process noise, which is modeled as a discrete-time zero-mean white sequence with covariance \mathbf{Q}_{clk} given by

$$\mathbf{Q}_{\text{clk}} \triangleq \mathbf{Q}_{\text{clk}_{\text{nav}}} + \mathbf{Q}_{\text{clk}_{\text{base}}},$$

$$\mathbf{Q}_{\text{clk}_i} \triangleq \begin{bmatrix} S_{\tilde{w}_{\delta t, i}} T + S_{\tilde{w}_{\dot{\delta} t, i}} \frac{T^3}{3} & S_{\tilde{w}_{\delta t, i}} \frac{T^2}{2} \\ S_{\tilde{w}_{\dot{\delta} t, i}} \frac{T^2}{2} & S_{\tilde{w}_{\delta t, i}} T \end{bmatrix},$$

where $i \in \{\text{nav}, \text{base}\}$, and $S_{\tilde{w}_{\delta t, i}}$ and $S_{\tilde{w}_{\dot{\delta} t, i}}$ are the clock bias and drift process noise power spectra, respectively. The values of $S_{\tilde{w}_{\delta t, i}}$ and $S_{\tilde{w}_{\dot{\delta} t, i}}$ depend on the clock's quality [37].

2) *EKF Time Update*: At time step k , the EKF produces an estimate of the state vector $\hat{\mathbf{x}}(k|j) \triangleq \mathbb{E}[\mathbf{x}(k)|\mathbf{Z}^j]$ along with an estimation error covariance $\mathbf{P}(k|j) \triangleq \mathbb{E}[\tilde{\mathbf{x}}(k|j)\tilde{\mathbf{x}}^T(k|j)]$, where $k \geq j$; $\mathbf{Z}^j \triangleq \{\mathbf{z}(l)\}_{l=1}^j$; and $\tilde{\mathbf{x}}(k|j) \triangleq \mathbf{x}(k) - \hat{\mathbf{x}}(k|j)$ is the estimation error.

The state estimate $\hat{\mathbf{x}}(k|j)$ can be written as

$$\hat{\mathbf{x}}(k|j) = [\hat{\mathbf{x}}_{\text{IMU}}^T(k|j), \hat{\mathbf{x}}_{\text{clk}}^T(k|j)]^T. \quad (5)$$

The evolution of b_{gz} and \mathbf{b}_a are modeled as random walk processes, i.e., $\dot{b}_{gz} = w_{gz}$ and $\dot{\mathbf{b}}_a = \mathbf{w}_a$ with $\mathbb{E}[w_{gz}] = 0$, $\mathbb{E}[\mathbf{w}_a] = \mathbf{0}$, $\text{cov}[w_{gz}] = \sigma_{w_{gz}}^2$, and $\text{cov}[\mathbf{w}_a] = \sigma_{w_a}^2 \mathbf{I}_{2 \times 2}$. The discrete-time update of the IMU states can be calculated via Euler integration as:

$$\begin{aligned} \hat{\theta}_z(k+1|j) &= \hat{\theta}_z(k|j) + T \left(\hat{\dot{\theta}}_z(k|j) - \hat{b}_{gz}(k|j) \right), \\ \hat{\mathbf{r}}(k+1|j) &= \hat{\mathbf{r}}(k|j) + \Delta \hat{\mathbf{r}}, \\ \hat{\mathbf{r}}(k+1|j) &= \hat{\mathbf{r}}(k|j) + T \hat{\dot{\mathbf{r}}}(k|j), \\ \hat{b}_{gz}(k+1|j) &= \hat{b}_{gz}(k|j), \\ \hat{\mathbf{b}}_a(k+1|j) &= \hat{\mathbf{b}}_a(k|j), \end{aligned}$$

where $\dot{\theta}_z$ is the angular rate around z -axis; T is the IMU sampling interval; $\Delta\hat{\mathbf{r}} = T\mathbf{R}^\top(\hat{\theta}_z(k|j))\left[\hat{\mathbf{r}}(k|j) - \hat{\mathbf{b}}_a(k|j)\right]$; $\hat{\mathbf{r}}$ is the acceleration along x - and y - axes; $\mathbf{z}_{\text{imu}} \triangleq [\dot{\theta}_{z_{\text{imu}}}, \mathbf{a}_{\text{imu}}^\top]^\top$ is the IMU measurement vector; $\mathbf{R}(\theta_z)$ is the rotation matrix representing the orientation of the body frame with respect to the global frame and is defined as

$$\mathbf{R}(\theta_z) \triangleq \begin{bmatrix} \cos \theta_z & \sin \theta_z \\ -\sin \theta_z & \cos \theta_z \end{bmatrix}.$$

The discrete-time update of the clock state estimate is given by

$$\hat{\mathbf{x}}_{\text{clk}}(k+1|j) = \mathbf{F}_{\text{clk}}\hat{\mathbf{x}}_{\text{clk}}(k|j), \quad (6)$$

The prediction error covariance matrix is given by

$$\mathbf{P}(k+1|j) = \mathbf{F}\mathbf{P}(k|j)\mathbf{F}^\top + \mathbf{Q}_d, \quad (7)$$

where $\mathbf{F} \triangleq \text{diag}[\mathbf{F}_{\text{IMU}}, \mathbf{F}_{\text{clk}}]$; $\mathbf{Q}_d = \text{diag}[\mathbf{Q}_{\text{IMU}}, \mathbf{Q}_{\text{clk}}]$; \mathbf{F}_{IMU} is the linearized discrete-time IMU state transition matrix given by

$$\mathbf{F}_{\text{IMU}} = \begin{bmatrix} 1 & \mathbf{0}_{1 \times 2} & \mathbf{0}_{1 \times 2} & \mathbf{0}_{1 \times 2} & T \\ \hat{\mathbf{S}}(k|j) & \mathbf{I}_{2 \times 2} & \mathbf{0}_{2 \times 2} & T\mathbf{R}(\theta_z(k|j)) & \mathbf{0}_{2 \times 1} \\ \mathbf{0}_{2 \times 1} & T\mathbf{I}_{2 \times 2} & \mathbf{I}_{2 \times 2} & \mathbf{0}_{2 \times 2} & \mathbf{0}_{2 \times 2} \\ \mathbf{0}_{2 \times 1} & \mathbf{0}_{2 \times 2} & \mathbf{0}_{2 \times 2} & \mathbf{I}_{2 \times 2} & \mathbf{0}_{2 \times 2} \\ 0 & \mathbf{0}_{1 \times 2} & \mathbf{0}_{1 \times 2} & \mathbf{0}_{1 \times 2} & 1 \end{bmatrix},$$

$$\hat{\mathbf{S}}(k|j) \triangleq \mathbf{J}\mathbf{R}[\hat{\theta}_z(k|j)] \left(\hat{\mathbf{r}}_{\text{IMU}}(k|j) + \hat{\mathbf{b}}_a(k|j) \right),$$

with $\mathbf{J} = \begin{bmatrix} 0 & 1 \\ -1 & 0 \end{bmatrix}$; \mathbf{Q}_{IMU} is the linearized discrete-time IMU state process noise covariance matrix given by

$$\mathbf{Q}_{\text{IMU}} = \frac{T}{2}\mathbf{F}_{\text{IMU}}^\top \mathbf{N}_c \mathbf{F}_{\text{IMU}} + \mathbf{N}_c,$$

where $\mathbf{N}_c \triangleq \mathbf{\Gamma}\mathbf{Q}_c\mathbf{\Gamma}^\top$; \mathbf{Q}_c is the continuous-time IMU process noise covariance matrix defined as

$$\mathbf{Q}_c = \text{diag} \left[\sigma_{g_z}^2, \sigma_a^2 \mathbf{I}_2, \sigma_{w_{g_z}}^2, \sigma_{w_a}^2 \mathbf{I}_2 \right];$$

and $\mathbf{\Gamma}$ is the error-state transition matrix defined as

$$\mathbf{\Gamma} = \begin{bmatrix} 1 & \mathbf{0}_{1 \times 2} & \mathbf{0}_{1 \times 3} \\ \mathbf{0}_{2 \times 1} & \mathbf{R}[\hat{\theta}_z(k|j)] & \mathbf{0}_{2 \times 3} \\ \mathbf{0}_{2 \times 1} & \mathbf{0}_{2 \times 2} & \mathbf{0}_{2 \times 3} \\ \mathbf{0}_{3 \times 1} & \mathbf{0}_{3 \times 2} & \mathbf{I}_{3 \times 3} \end{bmatrix}.$$

3) *EKF Measurement Update*: Once the EKF receives the base/navigator measurement vector \mathbf{z} , it performs a measurement update according to

$$\hat{\mathbf{x}}(k+1|k+1) = \hat{\mathbf{x}}(k+1|j) + \mathbf{K}(k+1)\boldsymbol{\nu}(k+1), \quad (8)$$

where $\boldsymbol{\nu}$ and \mathbf{K} are the innovation vector and Kalman gain, respectively, given by

$$\boldsymbol{\nu} \triangleq \mathbf{z} - \hat{\mathbf{z}},$$

$$\hat{\mathbf{z}}_u \triangleq \|\hat{\mathbf{r}}(k+1|j) - \mathbf{r}_{s_u}\|_2 + c\Delta\hat{t}(k+1|j),$$

$$\mathbf{K}(k+1) \triangleq \mathbf{P}(k+1|j)\mathbf{H}^\top(k+1)\mathbf{S}^{-1}(k+1),$$

$$\mathbf{S}(k+1) \triangleq \mathbf{H}(k+1)\mathbf{P}(k+1|j)\mathbf{H}(k+1)^\top + \mathbf{R}_n(k+1),$$

where $u = 1, \dots, U$ and \mathbf{R}_n is the measurement noise covariance matrix given by

$\mathbf{R}_n = \text{diag}[\sigma_{\text{nav}_1}^2 + \sigma_{\text{base}_1}^2, \dots, \sigma_{\text{nav}_U}^2 + \sigma_{\text{base}_U}^2]$ and \mathbf{H} is the Jacobian matrix defined as

$$\mathbf{H}(k+1) = \begin{bmatrix} \mathbf{H}^{(1)}(k+1) \\ \vdots \\ \mathbf{H}^{(U)}(k+1) \end{bmatrix},$$

$$\mathbf{H}^{(u)}(k+1) = \left[\mathbf{0}_{1 \times 3}, \frac{[\hat{\mathbf{r}}_u(k+1|j) - \mathbf{r}_{s_u}^u]^\top}{\|\hat{\mathbf{r}}_u(k+1|j) - \mathbf{r}_{s_u}^u\|_2}, \mathbf{0}_{1 \times 3}, 1, 0 \right].$$

The estimation error covariance matrix is updated according to

$$\mathbf{P}(k+1|k+1) = [\mathbf{I} - \mathbf{K}(k+1)\mathbf{H}]\mathbf{P}(k+1|j).$$

Note that the LTE navigator receiver's position was assumed to be identical to the IMU's position, i.e., $\mathbf{r}_{\text{nav}} \equiv \mathbf{r}$

V. EXPERIMENTAL RESULTS

To evaluate the performance of the proposed receiver and the base/navigator framework, an experiment was conducted in an indoor environment: Winston Chung Hall building at the University of California, Riverside. This section discusses the experimental setup, analyzes the performance of the code phase-based receiver and carrier phase-based receiver, and demonstrates the performance of the tightly-coupled LTE-IMU system.

A. Experimental Setup

The LTE base receiver was placed on the roof of the building, while the LTE navigator receiver was placed indoors. Both the base and navigator receivers were equipped with four consumer-grade cellular omnidirectional antennas to collect LTE data at four different carrier frequencies. These frequencies corresponded to three U.S. LTE cellular providers: T-Mobile, Verizon, and AT&T (note that two of the carrier frequencies were being used by the same provider). The base used three single-channel National Instruments (NI) universal software radio peripherals (USRPs)-2920 to simultaneously down-mix and synchronously sample LTE signals at 10 Msps. The signals were recorded on a laptop, which was connected to the USRPs through an ethernet cable. The base receiver's location was estimated using a GPS receiver.

The navigator receiver's hardware setup was similar to the base except for the USRP configurations, which were a dual-channel USRP-2954R and two USRPs-2920. The USRPs at the navigator receiver simultaneously down-mixed and synchronously sampled LTE signals at 20 Msps. The navigator receiver was equipped with a tactical-grade IMU (Septentrio AsteRx-i V [38]). The signals were processed in a post-processing fashion using MATLAB.

Several tags were placed at known locations on the ground before performing the experiment. Over the course of the experiment, a smart phone camera was used to record the location of the navigator using the tags on the ground, which were later used as the ground truth. Fig. 5 shows the base and navigator experimental hardware setup.

Fig. 6 shows the environmental layout of the experiment and the location of the eNodeBs to which the base and navigator receivers were listening.

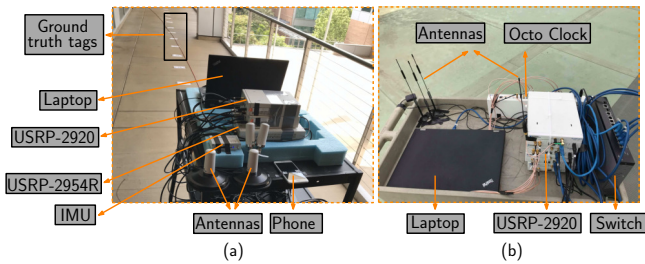


Fig. 5. (a) Navigator and (b) Base experimental hardware setup

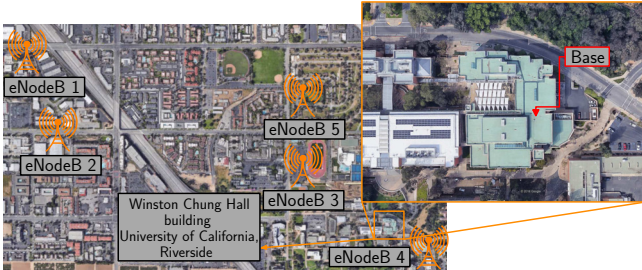


Fig. 6. The location of the LTE eNodeBs to which the base and navigator receivers were listening and the environmental layout of the experiment: Winston Chung Hall building at the University of California, Riverside. Image: Google Earth.

B. Code Phase-Based Receiver vs. Carrier Phase-Based Receiver

The objective of this subsection is to compare the performance of the code phase-based and the carrier phase-based receivers. The navigation observables of these two receivers were fed individually to an EKF to obtain their navigation solutions. The EKF used in this subsection did not use the IMU; instead, the EKF time-update used a velocity random walk dynamics as discussed in [24]. Fig. 7 shows the navigation solution for both receivers. The position RMSE of the carrier phase-based receiver was 5.09 m compared to 11.76 m for the code phase-based receiver.

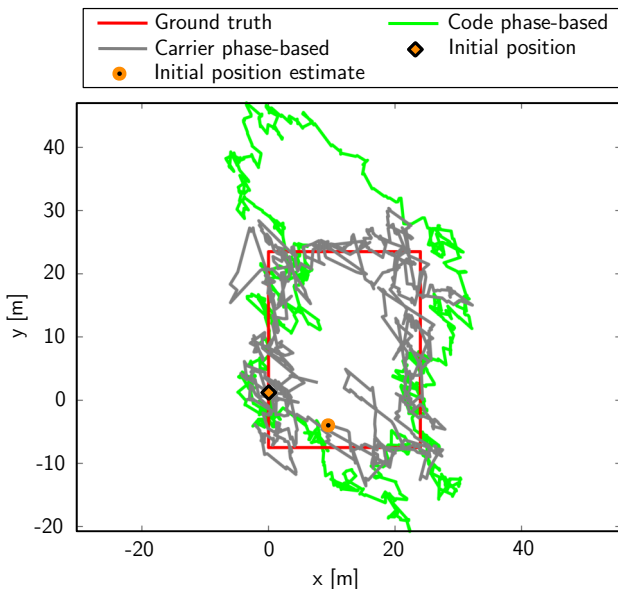


Fig. 7. The navigator's ground truth trajectory versus the standalone code phase-based and carrier phase-based receivers

It is worth noting the following remarks pertaining to the

results presented in Fig. 7.

Remark 1: In an indoor environment, short-delay multipath highly affects the received signal. Analytical results in [32] have shown that multipath can induce meter-level error in the code phase measurement, while this error is less than a wavelength (i.e., centimeter-level) for the carrier phase measurements. This is consistent with the carrier phase-based receiver outperforming the code phase-based receiver.

Remark 2: In a carrier phase-based receiver, the integer number of cycles from the transmitter to the receiver is ambiguous and must be estimated. Several algorithms have been proposed to estimate integer ambiguities [36]. In this paper, code phase measurements are used to initialize the integer ambiguities. Due to the low precision of code phase measurements, the accuracy of this approach is relatively lower compared to other integer ambiguity estimation algorithms.

Remark 3: Multipath can cause cycle slips in a carrier phase-based receiver, which must be detected and removed in order to achieve a reliable and accurate performance. Cycle slip detection is out of the scope of this paper.

C. Filter Initialization

The receiver's initial position and orientation are considered as the origin and orientation of the local frame in which the receiver's motion state is estimated. The gyroscope's and accelerometer's biases were initialized by taking the mean of 30 seconds of IMU data while the receiver was stationary.

The receiver's initial orientation, position, and velocity were initialized using a multivariate Gaussian random generator with a mean $\mathbb{E} \left\{ \left[\hat{\theta}_z(0|0), \hat{\mathbf{r}}^\top(0|0), \hat{\mathbf{v}}^\top(0|0) \right] \right\} = [0, 0, 0, 2.2, 0.2]$ and a covariance of $P(0|0) = \text{diag}[0.1, 100, 100, 10, 10]$.

The receiver's clock bias $c\Delta\delta t$ and drift $c\Delta\dot{\delta}t$ were initialized using the receiver's initial position and two consecutive prior measurements. The initial clock bias and drift uncertainties were set to 1 m^2 and 0.1 (m/s)^2 , respectively.

It is assumed that the receiver is equipped with a temperature-compensated crystal oscillator (TCXO); hence, the values of $S_{\tilde{w}_{\delta t, i}}$ and $S_{\tilde{w}_{\dot{\delta} t, i}}$ were set to 4.7×10^{-20} and 7.5×10^{-20} , respectively [37]. The measurement noise variance $\left\{ \sigma^2_{i, u} \right\}_{u=1}^U$ for $i \in \{\text{nav, base}\}$ were set to $\left\{ c^2 \frac{\alpha_u}{(C/N_0)_u} \right\}_{u=1}^U$, respectively, where $(C/N_0)_u$ is the received carrier-to-noise ratio for the u -th eNodeB and $\{\alpha_u > 0\}_{u=1}^U$ are tuning parameters that were chosen to be $\{5.56, 7.78, 3.33, 3.1, 3.78\} \times 10^{-12}$.

D. Navigation Results

In this subsection, the performance of the proposed navigation framework is evaluated. Over the course of experiment, the navigator receiver traversed a trajectory of 109 m, while the base was stationary. Fig. 8(a) shows the navigator's ground truth trajectory versus the navigation solution from: (1) IMU only, (2) standalone carrier phase-based LTE, and (3) LTE-IMU. Fig. 8(b) compares the navigation solution of the proposed LTE-IMU framework versus the ground truth. Table II summarizes the experimental results.

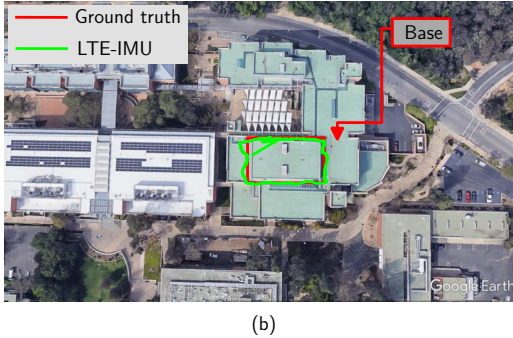
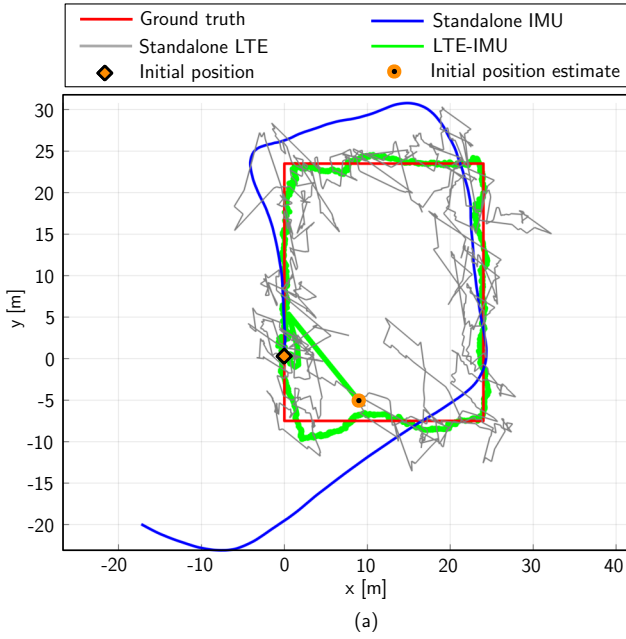


Fig. 8. The navigator's ground truth trajectory versus the navigation solution from: (1) IMU only, (2) standalone carrier phase-based LTE, and (3) LTE-IMU. Total traversed indoor trajectory was 109 m. Image: Google Earth.

Fig. 9 shows the EKF estimation error of the navigator's x -position and y -position along with the associated $\pm 2\sigma$ bounds.

TABLE II
INDOOR POSITIONING PERFORMANCE COMPARISON

Performance Measure [m]	IMU Only	Standalone LTE	LTE-IMU
RMSE	9.48	5.09	2.92
Standard deviation	10.36	5.66	2.74
Maximum error	22.53	14.24	5.60

VI. CONCLUSION

This paper evaluated the performance of two different LTE receivers for indoor localization: (1) code phase-based receiver and (2) carrier phase-based receiver. The experimental results with real LTE signals in an indoor environment showed that the carrier phase-based receiver outperforms the code phase-based receiver with a position RMSE of 5.09 m versus 11.76 m. A base/navigator navigation framework was proposed to remove the effect of the

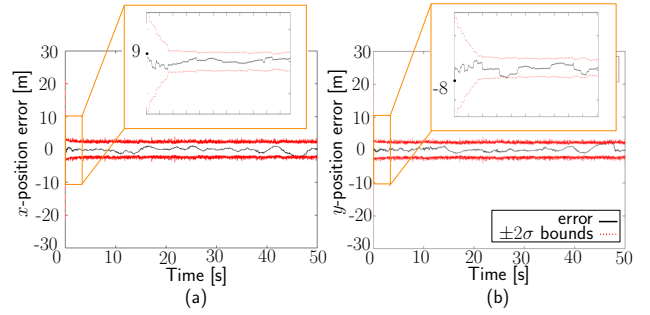


Fig. 9. EKF estimation error of the navigator's (a) x -position and (b) y -position along with the associated $\pm 2\sigma$ bounds.

unknown eNodeBs' clock biases. A tightly-coupled LTE-IMU system was presented to enable accurate indoor localization. The LTE-IMU navigation solution demonstrated a 2-D RMSE of 2.92 m and a maximum error of 5.6 m over 109 m trajectory. The 2-D position RMSE was improved by 69.2% when using the proposed LTE-IMU navigation framework compared to the IMU only solution.

ACKNOWLEDGMENT

The authors would like to thank Joe Khalife for his help in performing the experiments.

REFERENCES

- [1] Federal Communications Commission, "Wireless E911 location accuracy requirements," <https://apps.fcc.gov/edocspublic/attachmatch/FCC-15-9A1>, February 2015.
- [2] D. Ganti, W. Zhang, and M. Kavehrad, "VLC-based indoor positioning system with tracking capability using Kalman and particle filters," in *Proceedings of International Conference on Consumer Electronics*, January 2014, pp. 467–477.
- [3] S. Yang, E. Jeong, D. Kim, H. Kim, Y. Son, and S. Han, "Indoor three-dimensional location estimation based on LED visible light communication," *IEEE Electronics Letters*, vol. 49, no. 1, pp. 54–56, January 2013.
- [4] L. Ni, Y. Liu, Y. Lau, and A. Patil, "LANDMARC: indoor location sensing using active RFID," in *Proceedings of International Conference on Pervasive Computing and Communications*, March 2003, pp. 407–415.
- [5] A. Bekkali, H. Sanson, and M. Matsumoto, "RFID indoor positioning based on probabilistic RFID map and Kalman filtering," in *Proceedings of International Conference on Wireless and Mobile Computing, Networking and Communications*, October 2007, pp. 21–21.
- [6] C. Gentner, M. Ulmschneider, and T. Jost, "Cooperative simultaneous localization and mapping for pedestrians using low-cost ultra-wideband system and gyroscope," in *Proceedings of IEEE/ION Position Location and Navigation Symposium*, April 2018, pp. 1197–1205.
- [7] P. Groves, *Principles of GNSS, Inertial, and Multisensor Integrated Navigation Systems*, 2nd ed. Artech House, 2013.
- [8] M. Gallant and J. Marshall, "Two-dimensional axis mapping using LiDAR," *IEEE Transactions on Robotics*, vol. 32, no. 1, pp. 150–160, February 2016.
- [9] A. Mulloni, D. Wagner, I. Barakonyi, and D. Schmalstieg, "Indoor positioning and navigation with camera phones," *IEEE Pervasive Computing*, vol. 8, no. 2, pp. 22–31, April 2009.
- [10] J. McEllroy, "Navigation using signals of opportunity in the AM transmission band," Master's thesis, Air Force Institute of Technology, Wright-Patterson Air Force Base, Ohio, USA, 2006.
- [11] S. Fang, J. Chen, H. Huang, and T. Lin, "Is FM a RF-based positioning solution in a metropolitan-scale environment? A probabilistic approach with radio measurements analysis," *IEEE Transactions on Broadcasting*, vol. 55, no. 3, pp. 577–588, September 2009.
- [12] P. Thevenon, S. Damien, O. Julien, C. Macabiau, M. Bousquet, L. Ries, and S. Corazza, "Positioning using mobile TV based on the DVB-SH standard," *NAVIGATION, Journal of the Institute of Navigation*, vol. 58, no. 2, pp. 71–90, 2011.

- [13] J. Khalife, Z. Kassas, and S. Saab, "Indoor localization based on floor plans and power maps: Non-line of sight to virtual line of sight," in *Proceedings of ION GNSS Conference*, September 2015, pp. 2291–2300.
- [14] R. Faragher and R. Harle, "Towards an efficient, intelligent, opportunistic smartphone indoor positioning system," *NAVIGATION, Journal of the Institute of Navigation*, vol. 62, no. 1, pp. 55–72, 2015.
- [15] Z. Kassas, J. Khalife, K. Shamaei, and J. Morales, "I hear, therefore I know where I am: Compensating for GNSS limitations with cellular signals," *IEEE Signal Processing Magazine*, pp. 111–124, September 2017.
- [16] J. Khalife, K. Shamaei, and Z. Kassas, "Navigation with cellular CDMA signals – part I: Signal modeling and software-defined receiver design," *IEEE Transactions on Signal Processing*, vol. 66, no. 8, pp. 2191–2203, April 2018.
- [17] T. Reid, A. Neish, T. Walter, and P. Enge, "Broadband LEO constellations for navigation," *NAVIGATION, Journal of the Institute of Navigation*, vol. 65, no. 2, pp. 205–220, 2018.
- [18] J. Morales, J. Khalife, C. Ardito, and Z. Kassas, "Simultaneous tracking of Orbcomm LEO satellites and inertial navigation system aiding using Doppler measurements," in *Proceedings of IEEE Vehicular Technology Conference*, April 2019, pp. 1–6.
- [19] J. Khalife and Z. Kassas, "Receiver design for Doppler positioning with LEO satellites," in *Proceedings of IEEE International Conference on Acoustics, Speech and Signal Processing*, May 2019, pp. 5506–5510.
- [20] J. del Peral-Rosado, J. Lopez-Salcedo, G. Seco-Granados, F. Zanier, and M. Crisci, "Achievable localization accuracy of the positioning reference signal of 3GPP LTE," in *Proceedings of International Conference on Localization and GNSS*, June 2012, pp. 1–6.
- [21] K. Shamaei, J. Khalife, and Z. Kassas, "Pseudorange and multipath analysis of positioning with LTE secondary synchronization signals," in *Proceedings of Wireless Communications and Networking Conference*, 2018, pp. 286–291.
- [22] J. del Peral-Rosado, J. Lopez-Salcedo, G. Seco-Granados, F. Zanier, P. Crosta, R. Ioannides, and M. Crisci, "Software-defined radio LTE positioning receiver towards future hybrid localization systems," in *Proceedings of International Communication Satellite Systems Conference*, October 2013, pp. 14–17.
- [23] M. Driusso, C. Marshall, M. Sabathy, F. Knutti, H. Mathis, and F. Babich, "Vehicular position tracking using LTE signals," *IEEE Transactions on Vehicular Technology*, vol. 66, no. 4, pp. 3376–3391, April 2017.
- [24] K. Shamaei, J. Khalife, and Z. Kassas, "Exploiting LTE signals for navigation: Theory to implementation," *IEEE Transactions on Wireless Communications*, vol. 17, no. 4, pp. 2173–2189, April 2018.
- [25] C. Gentner, E. Munoz, M. Khider, E. Staudinger, S. Sand, and A. Dammann, "Particle filter based positioning with 3GPP-LTE in indoor environments," in *Proceedings of IEEE/ION Position, Location and Navigation Symposium*, April 2012, pp. 301–308.
- [26] M. Driusso, C. Marshall, M. Sabathy, F. Knutti, H. Mathis, and F. Babich, "Indoor positioning using LTE signals," in *Proceedings of International Conference on Indoor Positioning and Indoor Navigation*, October 2016, pp. 1–8.
- [27] F. Knutti, M. Sabathy, M. Driusso, H. Mathis, and C. Marshall, "Positioning using LTE signals," in *Proceedings of Navigation Conference in Europe*, April 2015, pp. 1–8.
- [28] K. Shamaei, J. Khalife, and Z. Kassas, "Comparative results for positioning with secondary synchronization signal versus cell specific reference signal in LTE systems," in *Proceedings of ION International Technical Meeting Conference*, January 2017, pp. 1256–1268.
- [29] A. Abdallah, K. Shamaei, and Z. Kassas, "Indoor positioning based on LTE carrier phase measurements and an inertial measurement unit," in *Proceedings of ION GNSS Conference*, September 2018, pp. 3374–3384.
- [30] K. Shamaei, , and Z. Kassas, "Sub-meter accurate UAV navigation and cycle slip detection with LTE carrier phase," in *Proceedings of ION GNSS Conference*, September 2019, accepted.
- [31] 3GPP, "Evolved universal terrestrial radio access (E-UTRA): physical channels and modulation," 3rd Generation Partnership Project (3GPP), TS 36.211, January 2011. [Online]. Available: <http://www.3gpp.org/ftp/Specs/html-info/36211.htm>
- [32] K. Shamaei and Z. Kassas, "LTE receiver design and multipath analysis for navigation in urban environments," *NAVIGATION, Journal of the Institute of Navigation*, vol. 65, no. 4, pp. 655–675, December 2018.
- [33] B. Yang, K. Letaief, R. Cheng, and Z. Cao, "Timing recovery for OFDM transmission," *IEEE Journal on Selected Areas in Communications*, vol. 18, no. 11, pp. 2278–2291, November 2000.
- [34] R. Roy and T. Kailath, "ESPRIT-estimation of signal parameters via rotational invariance techniques," *IEEE Transactions on Acoustics, Speech, and Signal Processing*, vol. 37, no. 7, pp. 984–995, July 1989.
- [35] E. Kaplan and C. Hegarty, *Understanding GPS: Principles and Applications*, 2nd ed. Artech House, 2005.
- [36] P. Misra and P. Enge, *Global Positioning System: Signals, Measurements, and Performance*, 2nd ed. Ganga-Jamuna Press, 2010.
- [37] Z. Kassas, V. Ghadiok, and T. Humphreys, "Adaptive estimation of signals of opportunity," in *Proceedings of ION GNSS Conference*, September 2014, pp. 1679–1689.
- [38] (2018) Septentrio AsteRx-i V. [Online]. Available: <https://www.septentrio.com/products>